

Context-Aware Deep Learning for Robust Channel Extrapolation in Fluid Antenna Systems

Yanliang Jin, Runze Yu, Yuan Gao, Shengli Liu, Xiaoli Chu, *Senior Member, IEEE*, Kai-Kit Wong, *Fellow, IEEE*, and Chan-Byoung Chae, *Fellow, IEEE*

Abstract—Fluid antenna systems (FAS) offer remarkable spatial flexibility but face significant challenges in acquiring high-resolution channel state information (CSI), leading to considerable overhead. To address this issue, we propose CANet, a robust deep learning model for channel extrapolation in FAS. CANet combines context-adaptive modeling with a cross-scale attention mechanism and is built on a ConvNeXt v2 backbone to improve extrapolation accuracy for unobserved antenna ports. To further enhance robustness, we introduce a novel spatial amplitude perturbation strategy, inspired by frequency-domain augmentation techniques in image processing. This motivates the incorporation of a Fourier-domain loss function, capturing frequency-domain consistency, alongside a spectral structure consistency loss that reinforces learning stability under perturbations. Our simulation results demonstrate that CANet outperforms benchmark models across a wide range of signal-to-noise ratio (SNR) levels.

Index Terms—Fluid antenna system (FAS), channel extrapolation, deep learning, amplitude perturbation.

I. INTRODUCTION

WITH the advent of sixth-generation (6G) mobile communications, the demand for higher capacity, wider coverage, and greater flexibility in wireless systems is accelerating. Meeting these ambitious requirements necessitates the development of advanced physical-layer technologies. Among them, the fluid antenna system (FAS) [1], [2] has emerged as a promising antenna architecture that introduces new spatial degrees of freedom (DoF) into wireless communication. FAS represents the capability of shape-and-position-reconfigurable antenna technology to empower the physical layer. By leveraging mechanical motion [3], liquid metals [4], reconfigurable pixel-based structures [5] or metamaterials [6], FAS enables dynamic port selection from a massive number of predefined locations. This adaptability facilitates spatial diversity gains in

The work of Y. Jin, R. Yu, Y. Gao and S. Liu is supported by the 6G Science and Technology Innovation and Future Industry Cultivation Special Project of Shanghai Municipal Science and Technology Commission under Grant 24DP1501001.

The work of K. K. Wong is supported by the Engineering and Physical Sciences Research Council (EPSRC) under Grant EP/W026813/1.

The work of C.-B. Chae was in part supported by the Institute for Information and Communication Technology Planning and Evaluation (IITP)/NRF grant funded by the Ministry of Science and ICT (MSIT), South Korea, under Grant RS-2024-00428780 and 2022R1A5A1027646.

Y. Jin, R. Yu, Y. Gao and S. Liu are with the School of Communication and Information Engineering, Shanghai University, China (e-mail: {jinyanliang, urleaves, gaoyuansie, victoryliu}@shu.edu.cn).

X. Chu is with the Department of Electronic and Electrical Engineering, the University of Sheffield, UK (e-mail: x.chu@sheffield.ac.uk).

K. K. Wong is with the Department of Electronic and Electrical Engineering, University College London, WC1E 7JE, United Kingdom, and also with Yonsei Frontier Lab, Yonsei University, Seoul, South Korea (e-mail: kai-kit.wong@ucl.ac.uk).

C.-B. Chae is with the School of Integrated Technology, Yonsei University, Seoul, 03722 South Korea (e-mail: cbchae@yonsei.ac.kr).

Corresponding author: Yuan Gao.

nearly continuous space and enhances the system's capability to respond intelligently to the wireless channel. In [7], Lu *et al.* explained FAS from the viewpoint of electromagnetics.

Since the introduction of FAS by Wong *et al.* in [8], [9], there have been lots of efforts in understanding the achievable performance of FAS [10], [11]. The use of FAS has also been considered for reconfigurable intelligent surface (RIS) systems [12], index modulation [13], [14], wideband communication [15], and integrated sensing and communication (ISAC) [16]. Capacity maximization for FAS channels has also been studied using statistical channel state information (CSI) [17] and instantaneous CSI [18]. The diversity-multiplexing trade-off for multiple-input multiple-output (MIMO) FAS channels was analyzed in [19].

Nonetheless, the promising performance of FAS relies on the availability of CSI and the high-resolution nature of FAS also leads to substantial overhead in acquiring CSI, including pilot overhead, feedback latency, and energy consumption [20]. In recent years, several studies explored the integration of physical modeling and data-driven approaches for CSI prediction [21], [22]. For instance, [23] proposed an inference algorithm to enable high-accuracy extrapolation in a massive FAS using only a small number of observed ports. Additionally, in [24], an extrapolation scheme based on masked language models, which reconstructs the full channel from a limited number of observed port CSI, was proposed. Going one step further, the approach in [25] integrates the diffusion mechanism of graph neural networks with an asymmetric masked autoencoder architecture, significantly improving both extrapolation accuracy and flexibility in high-resolution FAS settings. Prior to these, there were attempts that exploited channel sparsity [26] and used Bayesian approaches [27]. CSI prediction for multiuser FAS using deep learning was also reported in [28]. Overall, however, reliable CSI acquisition seems only possible at high signal-to-noise ratio (SNR) and it is important to study enhancement techniques that work well in noisy situations.

Motivated by the above, in this correspondence, we propose CANet, a novel deep learning framework designed for channel extrapolation in FAS. CANet adaptively infers the CSI of the unobserved ports with varying positions within a FAS, and maintains robust performance across different SNR scenarios. The architecture of CANet incorporates a context adaptive block (CAB), a cross-scale contextual attention (CSCA) mechanism, and a ConvNeXt v2 backbone enhanced with dropout regularization. This combination empowers CANet to process unobserved port positions both locally and globally, significantly improving the extraction of CSI features. To enhance model robustness further, we also introduce a spatial amplitude perturbation strategy. Besides, we refine the loss

function by incorporating a fast Fourier transform (FFT) loss, which collaborates with a spectral structure consistency loss to reinforce model stability. Numerical results indicate that CANet surpasses benchmark models, demonstrating superior channel extrapolation robustness across varying noise levels.

II. CHANNEL EXTRAPOLATION FOR FAS

Consider a downlink system where a base station (BS) with M_t fixed-position antennas (FPAs) communicates with U_t user terminals on the same time-frequency resource unit. Each user terminal employs a 2D FAS with $N_s = N_x \times N_y$ switchable positions (or ports), which are evenly distributed over a planar surface of physical dimensions $W_s = W_x \times W_y$. In a 3D rich scattering environment, the spatial correlation between port (n_x^s, n_y^s) and port $(\tilde{n}_x^s, \tilde{n}_y^s)$ is given by

$$J_{(n_x, n_y), (\tilde{n}_x, \tilde{n}_y)} = j_0 \left(\frac{2\pi}{\lambda} \sqrt{\left(\frac{|n_x - \tilde{n}_x|}{N_x - 1} W_x \right)^2 + \left(\frac{|n_y - \tilde{n}_y|}{N_y - 1} W_y \right)^2} \right), \quad (1)$$

where $j_0(\cdot)$ denotes the spherical Bessel function of the first kind, which can be approximated by $\text{sinc}(x) = \sin x/x$, and λ represents the carrier wavelength. The downlink channel for a typical user can then be modeled as

$$\mathbf{g} = \delta \mathbf{U}_s \sqrt{\mathbf{\Lambda}_s} \mathbf{G} + \mathbf{n}, \quad (2)$$

where $\mathbf{U}_s \in \mathbb{C}^{N_s \times N_s}$ and $\mathbf{\Lambda}_s \in \mathbb{C}^{N_s \times N_s}$ are defined in accordance with [19], representing the eigenvector matrix and eigenvalue diagonal matrix obtained from the eigen-decomposition of the spatial correlation matrix $\mathbf{J}_s = \mathbf{U}_s \mathbf{\Lambda}_s \mathbf{U}_s^H$, whose entries are given by (1). The matrix $\mathbf{G} \in \mathbb{C}^{N_s \times M_t}$ consists of independent complex Gaussian random variables with zero mean and variance of 1/2. The parameter δ characterizes the path loss, and \mathbf{n} is the additive white Gaussian noise.

III. PROPOSED APPROACH

Here, we propose CANet, a noise-robust architecture for the channel extrapolation task. We design a CAB to locally fuse the features of known CSI with weighted integration, while constraining the propagation of features from unknown CSI. To enhance global modeling capability, we introduce a CSCA module to facilitate feature completion for large unobserved port regions. Moreover, we adopt ConvNeXt v2 with dropout regularization to improve feature extraction and generalization after feature completion [29]. A spatial amplitude perturbation module is also incorporated to enhance the model's adaptability and robustness under various noise conditions.

A. Masking Strategy

We denote the perfect CSI as $\mathbf{g} \in \mathbb{C}^{N_s \times M_t}$, and construct a tensor $\mathbf{u} \in \mathbb{R}^{2M_t \times N_y \times N_x}$ to represent the concatenated real and imaginary components of the CSI across a 2D fluid antenna grid of size $N_x \times N_y$. To simulate partial observations, a subset of antenna ports is randomly masked along the spatial grid, with a masking ratio typically ranging from 80% to 95%. The resulting masked tensor is denoted as $\tilde{\mathbf{u}} \in \mathbb{R}^{2M_t \times N_y \times N_x}$, in which the unobserved positions are replaced with a distinct

negative value (e.g., -10) to make them distinguishable for the network. Additionally, we define a binary indicator matrix $\mathbf{E}_{\text{flag}} \in \{0, 1\}^{N_y \times N_x}$, where a value of 1 indicates an observed port and 0 is a masked (unobserved) port. No prior knowledge of the channel is used to select ports for extrapolation. Instead, a random masking strategy is employed to ensure flexibility and enhance the generalization capability of the model.

B. Model Architecture

The overall architecture of CANet consists of four training modules. Next, we summarize the role of each module.

1) *CAB*: For channel extrapolation tasks with strong spatial correlations, using convolutional neural network is a natural choice for feature extraction. However, conventional convolution is susceptible to interference from unobserved ports within the receptive field, which can degrade the quality of feature representations. To overcome this issue, we propose a dual-branch architecture that separately models and predicts the CSI of observed and unobserved ports, thereby enhancing both the modeling accuracy and the robustness of extrapolation.

Specifically, we first compute a soft mask (confidence map) over the entire feature map using convolution. This soft mask reflects the reliability of each feature.¹ Then we perform a weighted fusion of the outputs from the convolutional and attention branches to further refine feature extraction within the receptive field. For each pixel $x_o \in \mathbb{R}^C$ on the feature map $F \in \mathbb{R}^{C \times H \times W}$, its corresponding soft mask value m is computed by the following convolutional operation:

$$m = \sigma \left(\sum_{i \in \mathcal{B}_o} w_i^m x_i \right), \quad (3)$$

where σ denotes the sigmoid activation function, x_i represents the input features within the receptive field, w_i denotes learnable convolutional filters, and \mathcal{B}_o represents the receptive field range corresponding to filter w^m . The magnitude of m signifies the confidence level of the feature at that location. Conditioned on the learned soft mask m , we then introduce a self-attention mechanism [22] to derive a more contextually relevant feature representation x^a , given by

$$x^a = \sum_{i \in \mathcal{B}_o} \langle m w^q x_o, m w^k x_i \rangle m x_i w^v x_i, \quad (4)$$

where $\langle \cdot, \cdot \rangle$ denotes the composite operation of dot-product with softmax. This self-attention mechanism empowers the model to focus on context information pertinent to the current pixel, thereby enhancing the capability of features to capture and discriminate CSI. In parallel, within the convolutional branch, we employ another set of convolution kernels w^c to extract local channel features x^c by

$$m \in \sum_{i \in \mathcal{B}_o} w_i^c x_i. \quad (5)$$

¹Features affected by masked ports are assigned lower confidence, while those from observed regions receive higher confidence.

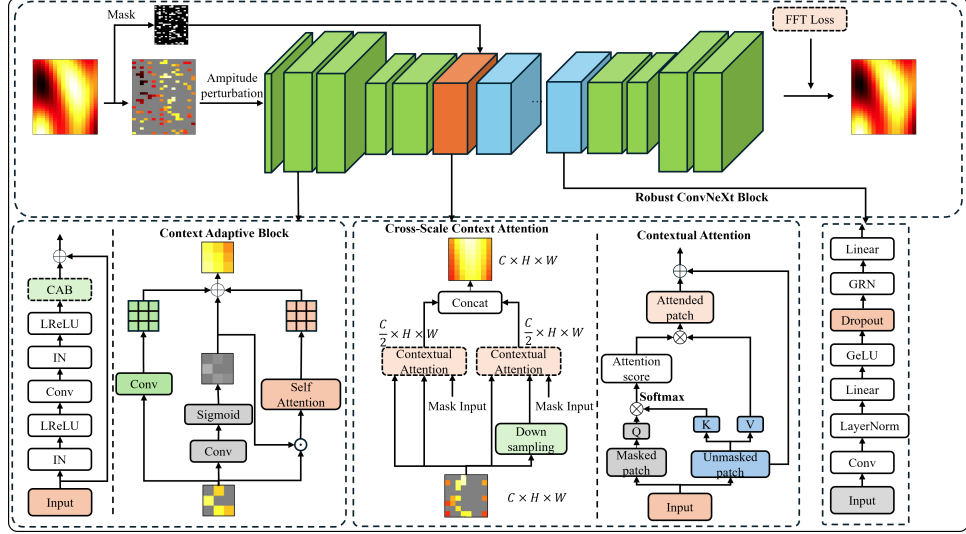


Fig. 1. The proposed CANet for CSI extrapolation in FAS channels, where \oplus , \otimes and \odot denote fuse, dot product and element-wise product, respectively.

Finally, we perform a weighted fusion of the convolutional branch output x_c and the attention branch output x_a based on the soft mask m , yielding the output

$$o = m \cdot x_c + (1 - m) \cdot x_a. \quad (6)$$

2) *CSCA*: In the CSCA module, we first reduce the input feature channels to half of the original before feeding them into two self-attention modules. One branch directly undergoes self-attention at the same scale, while the other duplicates the feature map and down-samples it to half of the original resolution. The downsampled feature map is then processed along with the original-scale features within the self-attention mechanism. At each self-attention stage, patches are extracted from the input features, and the cosine similarity between patches in the missing region and those in the external region is computed to establish cross-region feature correlations. Formally, let q_i denote the i -th patch from the observed region ψ^l , and k_j denote the j -th patch from the masked region ϕ^l . The cosine similarity is computed as

$$s_{i,j} = \left\langle \frac{q_i}{\|q_i\|}, \frac{k_j}{\|k_j\|} \right\rangle. \quad (7)$$

The attention weights are then computed by

$$a_{i,j} = \frac{\exp(s_{i,j})}{\sum_j \exp(s_{i,j})}. \quad (8)$$

The unobserved port patches are then reconstructed based on the computed attention scores, given by

$$\hat{q} = \sum_j a_{i,j} v_j, \quad (9)$$

where v_j represents the j -th patch extracted from features outside unobserved regions. Finally we concatenate the results of the two branches as the final result.

3) *ConvNeXt v2 with dropout regularization*: After CAB and CSCA, we adopt ConvNeXt V2 [29] with dropout regularization as the backbone network to further enhance feature extraction and improve generalization. ConvNeXt has been

widely used for its strong feature representation capabilities, and ConvNeXt V2 builds upon this by introducing the global response normalization (GRN) module, which enables more expressive feature representations. In our design, we employ the ConvNeXt V2 block for channel extrapolation. By randomly dropping a subset of neurons during training, dropout alters the effective network structure in each training epoch, leading to a degree of statistical independence across different training instances, thereby reducing prediction variance and enhancing generalization under diverse noise conditions.

4) *Spatial amplitude perturbation*: To enhance the model's robustness, we propose a spatial amplitude perturbation strategy at the input stage, inspired by frequency perturbation techniques in the image domain [30], [31]. Specifically, the input CSI features are first zero-mean normalized to remove the DC component, then transformed into the frequency domain via FFT. The amplitude spectrum is then perturbed in a stochastic manner based on a predefined probability, effectively simulating potential frequency interference and noise. This approach improves the model's adaptability to unseen distributions:

$$\tilde{\mathbf{z}} = \tilde{\mathbf{u}} - \frac{1}{HW} \sum_{h=1}^H \sum_{w=1}^W \tilde{\mathbf{u}}_{h,w}. \quad (10)$$

$$\hat{\mathbf{z}} = \mathcal{F}^{-1}(\mathcal{F}(\tilde{\mathbf{z}}) \cdot (1 + \gamma \cdot \xi \cdot \delta)) + \bar{\mathbf{z}}, \quad (11)$$

where $\tilde{\mathbf{z}}$ is the spatially zero-mean feature, $\hat{\mathbf{z}}$ is the final perturbed feature after reconstruction, $\mathcal{F}(\cdot)$ and $\mathcal{F}^{-1}(\cdot)$ denote the 2D discrete Fourier transform and its inverse. The perturbation mask $\delta \in \{0, 1\}^{H \times W}$ above is sampled from a Bernoulli distribution with probability μ , and the amplitude coefficients $\xi \in [0, 1]^{H \times W}$ are sampled from a normal distribution $\mathcal{N}(0, 1)$. The hyperparameters μ and γ control the perturbation probability and maximum strength, respectively. Only the amplitude of each frequency component is perturbed, while the phase is fixed to maintain structural consistency.

5) *Loss Function*: Since the CSI tensor is represented by concatenating the real and imaginary parts, we reconstruct it

TABLE I
ARCHITECTURE OF THE PROPOSED CANET

Layer	Operator	Input Size	Output Size	Output Channel	Kernel Size	Stride	Nonlinearity
1	CAB	32×16	32×16	64	5	1	LeakyReLU
2	CAB	32×16	32×16	128	3	2	LeakyReLU
3	CAB	32×16	16×8	128	3	1	LeakyReLU
4	CAB	16×8	16×8	256	3	1	LeakyReLU
5	CAB	16×8	16×8	256	3	1	LeakyReLU
6	CSCA	16×8	16×8	256	Null	Null	Null
7-16	ConvNeXt v2	16×8	16×8	256	7	3	GeLU
17	BilinerUp	16×8	32×16	256	3	1	Null
18	CAB	32×16	32×16	128	3	1	LeakyReLU
19	CAB	32×16	32×16	128	3	1	LeakyReLU
20	CAB	32×16	32×16	64	3	1	LeakyReLU
21	CAB	32×16	32×16	64	3	1	LeakyReLU
22	Conv	32×16	32×16	16	7	1	Null

into a complex-valued tensor before computing the frequency-domain loss to enable the 2D Fourier transform. We denote the original CSI tensor as $\mathbf{U}_c \in \mathbb{R}^{M_t \times N_y \times N_x}$, and $\hat{\mathbf{U}}_c \in \mathbb{R}^{M_t \times N_y \times N_x}$ denote the predicted CSI recovered from the masked input $\tilde{\mathbf{U}}_c$. Let $\Omega \subset \{1, \dots, N_y\} \times \{1, \dots, N_x\}$ denote the set of unobserved spatial locations, with $|\Omega| = N_a$. The total loss is then defined as

$$\mathcal{L}_{\text{total}} = \mathcal{L}_{\text{MSE}} + \beta \mathcal{L}_{\text{FFT}}, \quad (12)$$

where \mathcal{L}_{MSE} and \mathcal{L}_{FFT} are the mean-square-error (MSE) loss and the FFT loss attributed to spatial amplitude perturbation, respectively, calculated as

$$\mathcal{L}_{\text{MSE}} = \mathbb{E} \left[\frac{1}{|\Omega|} \sum_{(y,x) \in \Omega} \left\| \hat{\mathbf{U}}_c[:, y, x] - \mathbf{U}_c[:, y, x] \right\|_2^2 \right], \quad (13)$$

$$\mathcal{L}_{\text{FFT}} = \mathbb{E} \left[\left\| \left| \mathcal{F}(\hat{\mathbf{U}}_c) \right| - \left| \mathcal{F}(\mathbf{U}_c) \right| \right\|_2^2 \right], \quad (14)$$

in which β balances the contribution of the two losses. The FFT loss enforces global consistency in the spatial frequency domain, which helps preserve large-scale channel structure.

IV. NUMERICAL RESULTS

In the simulations, the FAS channel involves U_t users. Each user has a planar FAS of size W_s cm² and N_s antenna ports. We assume $m_t = U_t$, and the BS is equipped with M_t FPAs. The carrier frequency is 3.4 GHz. Detailed simulation parameters are summarized in Table I. The dataset used for analysis contains a total of 310,000 samples, divided into 240,000 training samples, 60,000 validation samples, and 10,000 test samples for model training and performance evaluation. The total number of ports at the FAS side is set to $N_s = 512$.

The performance is evaluated through the normalized MSE (NMSE), defined as

$$\text{NMSE}(\hat{\mathbf{g}}, \mathbf{g}) = \frac{\sum_{n=1}^{N_{\text{test}}} \|\mathbf{g}_n - \hat{\mathbf{g}}_n\|^2}{\sum_{n=1}^{N_{\text{test}}} \|\mathbf{g}_n\|^2}, \quad (15)$$

where N_{test} denotes the number of test samples. The predicted CSI matrix $\hat{\mathbf{g}}$ is obtained by rearranging the extrapolated tensor $\hat{\mathbf{U}}_c$ into the standard CSI format. The batch size used in training is set to 32. The initial learning rate is 0.0005. For optimization, the AdamW optimizer is employed with the

parameters $\beta_1 = 0.9$, $\beta_2 = 0.999$, and the weight decay set to 0.0001. We set the maximum strength γ to 0.5, μ to 0.05, and the dropout rate to 0.5, β to 0.02.

Figs. 2(a) and 2(b) illustrate the NMSE curves of different models under various SNR conditions, as a function of the observed port ratio, for FAS sizes of 2 cm \times 4 cm and 8 cm \times 16 cm, respectively. We reproduce the AGMAE in [25] as a baseline for comparison. The simplified version of CANet without spatial amplitude perturbation and spectral consistency loss is denoted as ‘CANet-B’, while the full CANet model includes all the proposed components. In the figures, curves with the same line style represent the same SNR setting.

The results demonstrate that as the ratio of observed ports increases, the NMSE of all the models decreases considerably, showing that richer observed information leads to better reconstruction performance. Under extremely low observation rates (e.g., 5%), AGMAE slightly outperforms CANet-B, suggesting that its structure has certain advantages under highly sparse inputs. But in most observation rates, CANet-B consistently surpasses AGMAE. Furthermore, with the incorporation of amplitude spectrum perturbation and spectral consistency loss, the overall performance of CANet is further improved. For example, at an observation rate of 20% with the 2 cm \times 4 cm FAS, CANet achieves up to a 3 dB NMSE gain over CANet-B, demonstrating stronger noise robustness and generalization ability. Fig. 2(b) shows a similar trend under a larger FAS size, validating the adaptability and effectiveness of the proposed method across different physical FAS configurations.

V. CONCLUSIONS

In this correspondence, we proposed CANet, a robust CSI extrapolation model that excels in processing unobserved port positions in FAS. CANet integrates a CAB, CSCA, and a ConvNeXt v2 backbone. This combination allows for adaptive CSI feature extraction at both local and global levels. A spatial amplitude perturbation strategy was also proposed to enhance the loss function with an FFT loss. Our simulation results indicated that CANet consistently outperforms benchmark models, demonstrating improved accuracy and remarkable robustness in channel extrapolation under various noise conditions.

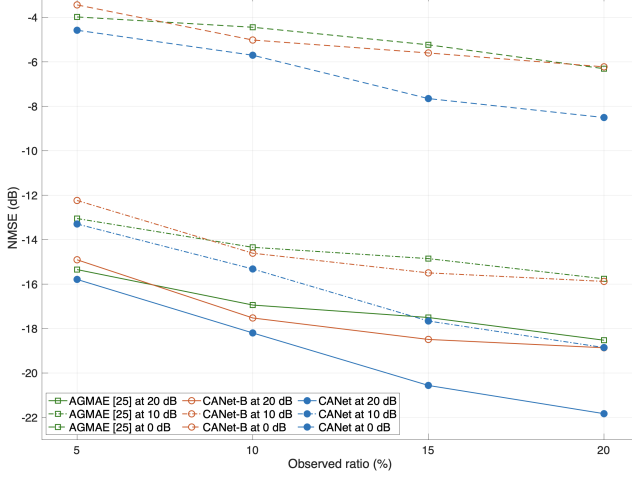
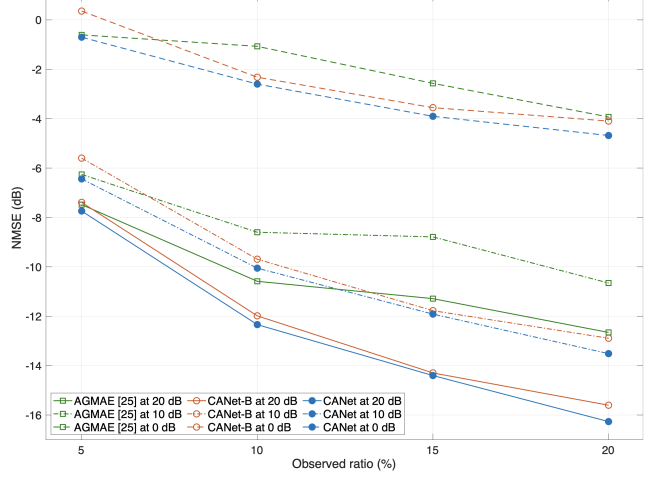
(a) $W_s = 2 \text{ cm} \times 4 \text{ cm}$ (b) $W_s = 8 \text{ cm} \times 16 \text{ cm}$

Fig. 2. NMSE versus the number of observed ports with different FAS sizes.

REFERENCES

- [1] K.-K. Wong, K.-F. Tong, Y. Shen, Y. Chen, and Y. Zhang, "Bruce Lee-inspired fluid antenna system: Six research topics and the potentials for 6G," *Frontiers Commun. Netw.*, vol. 3, Mar. 2022, art. no. 853416.
- [2] W. K. New *et al.*, "A tutorial on fluid antenna system for 6G networks: Encompassing communication theory, optimization methods and hardware designs," *IEEE Commun. Surv. Tuts.*, 2024, early access, doi:10.1109/COMST.2024.3498855.
- [3] S. Basbug, "Design and synthesis of antenna array with movable elements along semicircular paths," *IEEE Antennas Wireless Propag. Lett.*, vol. 16, pp. 3059–3062, Oct. 2017.
- [4] Y. Shen *et al.*, "Design and implementation of mmwave surface wave enabled fluid antennas and experimental results for fluid antenna multiple access," *arXiv:2405.09663*, May 2024, arXiv preprint.
- [5] J. Zhang *et al.*, "A novel pixel-based reconfigurable antenna applied in fluid antenna systems with high switching speed," *IEEE Open J. Antennas & Propag.*, vol. 6, no. 1, pp. 212–228, Feb. 2025.
- [6] B. Liu, K. F. Tong, K. K. Wong, C.-B. Chae, and H. Wong, "Be water, my antennas: Riding on radio wave fluctuation in nature for spatial multiplexing using programmable meta-fluid antenna," *arXiv:2502.04693*, Feb. 2025, arXiv preprint.
- [7] W.-J. Lu *et al.*, "Fluid antennas: Reshaping intrinsic properties for flexible radiation characteristics in intelligent wireless networks," *IEEE Commun. Mag.*, vol. 63, no. 5, pp. 40–45, May 2025.
- [8] K. K. Wong, A. Shojaeifard, K. F. Tong, and Y. Zhang, "Performance limits of fluid antenna systems," *IEEE Commun. Lett.*, vol. 24, no. 11, pp. 2469–2472, Nov. 2020.
- [9] K. K. Wong, A. Shojaeifard, K. F. Tong, and Y. Zhang, "Fluid antenna systems," *IEEE Trans. Wireless Commun.*, vol. 20, no. 3, pp. 1950–1962, Mar. 2021.
- [10] W. K. New, K. K. Wong, H. Xu, K. F. Tong, and C. B. Chae, "Fluid antenna system: New insights on outage probability and diversity gain," *IEEE Trans. Wireless Commun.*, vol. 23, no. 1, pp. 128–140, Jan. 2024.
- [11] P. Ramírez-Espinosa, D. Morales-Jimenez, and K. K. Wong, "A new spatial block-correlation model for fluid antenna systems," *IEEE Trans. Wireless Commun.*, vol. 23, no. 11, pp. 15 829–15 843, Nov. 2024.
- [12] X. Lai *et al.*, "FAS-RIS: A block-correlation model analysis," *IEEE Trans. Veh. Technol.*, vol. 74, no. 2, pp. 3412–3417, Feb. 2025.
- [13] J. Zhu *et al.*, "Index modulation for fluid antenna-assisted mimo communications: System design and performance analysis," *IEEE Trans. Wireless Commun.*, vol. 23, no. 8, pp. 9701–9713, Aug. 2024.
- [14] J. Zhu *et al.*, "Fluid antenna empowered index modulation for RIS-aided mmWave transmissions," *IEEE Trans. Wireless Commun.*, vol. 24, no. 2, pp. 1635–1647, Feb. 2025.
- [15] H. Hong *et al.*, "Downlink OFDM-FAMA in 5G-NR systems," *IEEE Trans. Wireless Commun.*, 2025, *arXiv:2501.06974*.
- [16] C. Wang *et al.*, "Fluid antenna system liberating multiuser MIMO for ISAC via deep reinforcement learning," *IEEE Trans. Wireless Commun.*, vol. 23, no. 9, pp. 10 879–10 894, Sep. 2024.
- [17] Y. Ye *et al.*, "Fluid antenna-assisted MIMO transmission exploiting statistical CSI," *IEEE Commun. Lett.*, vol. 28, no. 1, pp. 223–227, Jan. 2024.
- [18] C. N. Efrém and I. Krikidis, "Transmit and receive antenna port selection for channel capacity maximization in fluid-MIMO systems," *IEEE Wireless Commun. Lett.*, vol. 13, no. 11, pp. 3202–3206, Nov. 2024.
- [19] W. K. New, K.-K. Wong, H. Xu, K.-F. Tong, and C.-B. Chae, "An information-theoretic characterization of MIMO-FAS: Optimization, diversity-multiplexing tradeoff and q -outage capacity," *IEEE Trans. Wireless Commun.*, vol. 23, no. 6, pp. 5541–5556, Jun. 2024.
- [20] Y. Gao, X. Xu, Y. Jin, W. Yuan, J. Zhang, and S. Xu, "Joint channel estimation and data detection for OTFS systems: A lightweight deep learning framework with a novel data augmentation method," *IEEE Internet of Things Journal*, 2025.
- [21] Y. Gao, X. Wu, Y. Gao, and S. Xu, "C2S: An Transformer-based framework to extrapolate sensing channel from communication channel," in *2024 IEEE 100th Vehicular Technology Conference (VTC2024-Fall)*. IEEE, 2024, pp. 1–5.
- [22] Y. Jin, Y. Wu, Y. Gao, S. Zhang, S. Xu, and C.-X. Wang, "Linformer: A linear-based lightweight transformer architecture for time-aware mimo channel prediction," *IEEE Transactions on Wireless Communications*, 2025.
- [23] G. Li, H. Zhang, C. Wang, and B. Wang, "Model-driven channel extrapolation for massive fluid antenna," in *Proc. IEEE Int. Conf. Commun. Workshops (ICC Workshops)*, Denver, CO, USA, Jun. 2024, pp. 1146–1151.
- [24] X. Wu, H. Zhang, C.-C. Wang, and Z. Li, "Channel state information extrapolation in fluid antenna systems based on masked language model," in *Proc. IEEE Int. Conf. Commun. Workshops (ICC Workshops)*, Denver, CO, USA, Jun. 2024, pp. 1383–1388.
- [25] H. Zhang *et al.*, "Learning-induced channel extrapolation for fluid antenna systems using asymmetric graph masked autoencoder," *IEEE Wireless Commun. Lett.*, vol. 13, no. 6, pp. 1665–1669, Jun. 2024.
- [26] W. K. New *et al.*, "Channel estimation and reconstruction in fluid antenna system: Oversampling is essential," *IEEE Trans. Wireless Commun.*, vol. 24, no. 1, pp. 309–322, Jan. 2025.
- [27] B. Xu, Y. Chen, Q. Cui, X. Tao, and K. K. Wong, "Sparse bayesian learning-based channel estimation for fluid antenna systems," *IEEE Wireless Commun. Lett.*, vol. 14, no. 2, pp. 325–329, Feb. 2025.
- [28] N. Waqar, K.-K. Wong, K.-F. Tong, A. Sharples, and Y. Zhang, "Deep learning enabled slow fluid antenna multiple access," *IEEE Commun. Lett.*, vol. 27, no. 3, pp. 861–865, Mar. 2023.
- [29] S. Woo *et al.*, "Convnext V2: Co-designing and scaling convnets with masked autoencoders," in *Proc. IEEE/CVF Conf. Comput. Vision & Pattern Recognition (CVPR)*, Vancouver, BC, Canada, Jun. 2023, pp. 16 133–16 142.
- [30] C. Liu, Y. Cao, X. Su, and H. Zhu, "Universal frequency domain perturbation for single-source domain generalization," in *Proc. ACM Int. Conf. Multimedia*, Melbourne, Australia, Oct. 2024, pp. 6250–6259.

- [31] Z. Yang and C. Yu, "A single source generalization model via spatial amplitude perturbation and sensitivity guidance for colored medical image segmentation," in *Proc. Int. Conf. Pattern Recognition*, Kolkata, India, Dec. 2024.
- [32] F. R. Ghadi *et al.*, "Physical layer security over fluid antenna systems: Secrecy performance analysis," *IEEE Trans. Wireless Commun.*, vol. 23, no. 12, pp. 18 201–18 213, Dec. 2024.
- [33] H. Xu *et al.*, "Channel estimation for FAS-assisted multiuser mmWave systems," *IEEE Commun. Lett.*, vol. 28, no. 3, pp. 632–636, Mar. 2024.
- [34] Z. Zhang, J. Zhu, L. Dai, and R. W. H. Jr, "Successive bayesian reconstructor for channel estimation in fluid antenna systems," *IEEE Trans. Wireless Commun.*, vol. 24, no. 3, pp. 1992–2006, Mar. 2025.